



# 3D nanoprinted kinoform spiral zone plates on fiber facets for high-efficiency focused vortex beam generation

JIAN YU,<sup>1,2</sup> ZHIYONG BAI,<sup>2,3</sup>  GUOXUAN ZHU,<sup>1,2</sup> CAILING FU,<sup>2,3</sup>   
YALI LI,<sup>2</sup> SHEN LIU,<sup>2</sup> CHANGRUI LIAO,<sup>2,3</sup>  AND YIPING WANG<sup>1,2,3,\*</sup>

<sup>1</sup>Key Laboratory of Optoelectronic Devices and Systems of Ministry of Education and Guangdong Province, Shenzhen University, Shenzhen 518060, China

<sup>2</sup>Guangdong and Hong Kong Joint Research Centre for Optical Fibre Sensors, College of Physics and Optoelectronic Engineering, Shenzhen University, Shenzhen 518060, China

<sup>3</sup>Shenzhen Photonic Sensing Technology Co., Ltd, Shenzhen 518100, China

\*ypwang@szu.edu.cn

**Abstract:** In this paper, we propose and demonstrate an all-fiber high-efficiency focused vortex beam generator. The generator is fabricated by integrating a kinoform spiral zone plate (KSZP) on the top of the composite fiber structure using fs-laser two-photon polymerization 3D nanoprinting. The KSZP with spiral continuous-surface relief feature is designed by superimposing a spiral phase into a kinoform lens, which can efficiently concentrate and transform an all incident beam to a single-focus vortex beam, without the undesired zero-order diffracted light and extra high-order focus. Under arbitrary polarized light incident conditions, experiment results show that the focusing efficiency and vortex purity of the all-fiber generators are over 60% and 86%, respectively, which is much higher than that of a traditional binary SZP integrated on an optical fiber facet. In addition, characteristics of the generated vortex beam, such as focal spot, focal length and vortex topological charge are numerically designed and experimentally investigated. The experimental results agree well with the numerical simulation model using the FDTD algorithm. Due to the compact size, flexible design, polarization insensitivity, high focusing efficiency and high vortex purity, the proposed all-fiber photonic devices have promising potential in optical communication, particle manipulation and quantum computation applications.

© 2020 Optical Society of America under the terms of the [OSA Open Access Publishing Agreement](#)

## 1. Introduction

Optical vortices have been an enticing topic for theoretical and applied research due to unique optical properties such as the helical wavefront and orbital angular momentum (OAM) [1]. It has been widely applied in fields of laser communication [2,3], super resolution microscopy [4,5], kinematic micromanipulation [6] and quantum information processing [7]. Nowadays, various methods have emerged to generate this kind of unique beam, such as cylindrical mode converter [8], spiral phase plate [9], metasurface [10], and spatial light modulator [11]. Especially, the vortex beam generation based on diffractive optical elements has been widely accepted for their low cost, light weight, easy integration, etc. Furthermore, these diffractive optical elements have only a wavelength-level thickness and have played a crucial role in the optical communication and interconnection applications of vortex beams.

Up to now, a great of effort have been devoted to directly generating focused vortex beams for various applications, such as vortex optical tweezers [12,13] and super-resolution imaging [14]. The spiral zone plate (SZP) is a typical hybrid diffractive optical element and was first proposed by Heckenberg *et al.* to generate a focused vortex beam [15]. It can be considered as a simple combination of spiral phase plate and Fresnel zone plate (FZP) [16]. However, similar to a FZP [17], the conventional SZP is a binary diffractive element and its focusing efficiency

is only up to 10% of the incident beams. In addition to the desired 1st order focus for their design, the beam energy transmitted from SZP is also dispersed into its zero-order and extra multiple high-order focuses [18]. This undesired light not only seriously reduces the energy efficiency, but also causes a high background noise. In addition, the vortex topological charge of the high-order focus is several times that of the 1st order focus. Therefore, the vortex purity of the output beam is very low due to the coaxial transmission of all diffracted light. Although SZP has been invented for many years, its low focusing efficiency and vortex purity at the designed focus position limit its use in micro-optical systems.

To improve the focusing efficiency of diffractive elements, many methods have been reported, such as the stratified volume diffraction [19], total internal reflection [20], staircase microstructures [21], polarization modulating structures [22], and optical meta-surfaces [23]. Taking the form of a kinoform lens is the most direct and reliable method for high-efficiency focusing diffractive element [24,25]. Focusing efficiency of the kinoform-lens-based on devices depends on the continuity of surface relief profile of the purely phase shift material. In theory, the perfect continuous-surface relief profile can make the kinoform lenses to achieve an extremely high focusing efficiency of 100%. Various fabrication technologies including e-beam lithography [26], gray-scale focused ion beam lithography [27–29], and laser-induced refractive index modification [30,31] have been used to realize this diffractive optical elements on different substrate materials (e.g., Sapphire [30] and Silicon nitride membrane [27]). However, these traditional technologies have low processing efficiency, and the optical performance of processed elements is greatly affected by the inclination and flatness of substrate material.

Recently, the way to produce arbitrary geometry structures with sub-micrometer scale based on two-photon polymerization (TPP) has emerged thanks to advances in materials chemistry and laser technology [32–35]. The powerful preparation technique uses nonlinear absorption of the photons from an intense infrared fs-laser source to produce a subwavelength interaction volume down to a few tens of nanometers [36,37]. Therefore, prepared geometrical structures are in perfect agreement with the theoretical design and give the structures excellent optical properties. For example, from the perspective of using SZP to efficiently generate focused vortex beams, the fabrication of Gabor SZP with cosine continuous-surface on SU-8 photoresist by fs-laser TPP nanoprinting was proposed by Tian *et al.* to realize a single-focus [38]. Similarly, a high-performance multi-OAM generator with a hybrid continuous-surface profile was also fabricated by Hu *et al.* via the same processing technology for the generation of multiple vortex beams along the optical axis [39]. In addition, a commercially available two-photon polymerization micro-nano processing system was equipped the galvo-mirror subsystem to control the fs-laser deflection enabling a fast 3D nanoprinting [40].

The rapid progress in the fs-laser 3D nanoprinting technology based on the TPP mechanism has aroused widespread interest in the design and preparation of high-efficiency micro-nano diffractive optical elements. Based on this processing technology, we prepare a kinoform spiral zone plate (KSZP) on the top of the composite fiber structure composed of a single mode fiber and a quarter pitch graded index fiber in this paper. The KSZP has a spiral continuous-surface relief structure, and it was designed by superimposing a spiral phase into the traditional kinoform lens. Due to its unique optical modulation effect, the light propagating inside optical fiber can be converted into a single-focus vortex beam with high focusing efficiency and vortex purity. We believe that the proposed photonic device will be a promise all-fiber focused vortex beam generator. It can be used in fields of OAM optical communication, particle manipulation and quantum computing. Firstly, we introduce the theoretical design method and experimental preparation process of the all-fiber generators. Then, we investigate their output characteristics such as focal spot, focal length, vortex topological charge, focusing efficiency, and vortex purity by numerical simulation and experiment.

## 2. Theoretical design and experimental preparation

The schematic of all-fiber generator is shown in Fig. 1(a). We first spliced an 80 mm long single mode fiber (SMF) (8.2/125  $\mu\text{m}$ , Corning G652D) to a segment of graded-index multimode fiber (GIF) (62.5/125  $\mu\text{m}$ , Yangtze Optical Fiber GI0.275). And then, the GIF was cut to a quarter-pitch length ( $245 \pm 3 \mu\text{m}$ ) with a computer-controlled fiber precision cleaving system [41]. Subsequently, the KSZP with a cylindrical base was polymerized onto the GIF facet using fs-laser nanoprinting technology. In theory, the light propagating in the SMF will be expanded and collimated in the GIF segment, and then the polymerized KSZP will convert the collimated beam to a single-focus vortex beam. The KSZP was designed with an operating laser wavelength  $\lambda = 1550 \text{ nm}$ , focal length  $f = 30 \mu\text{m}$ , and diameter size  $D = 62.5 \mu\text{m}$ . Its phase function can be considered as the phase function product of spiral phase plate and traditional kinoform lens, expressed as follows [38]

$$\varphi_{KSZP_\ell}(r, \varphi) = \ell\varphi - \frac{\pi r^2}{\lambda f}, \quad (1)$$

where  $\ell$  represents the microstructure topological charge (or the number of spiral arms), and  $(r, \varphi)$  refer to the polar coordinates. The polymerized KSZP has the height profile of

$$h_{KSZP_\ell}(r, \varphi) = \frac{\lambda}{2\pi(n_m - n_{air})} \text{mod} [\varphi_{KSZP_\ell}(r, \varphi), 2\pi] + h_0, \quad (2)$$

where  $n_m$  and  $n_{air}$  are the refractive indices of KSZP material and surrounding air, respectively. The refractive index  $n_m$  was set to 1.48, which mainly refers to the experimental data in literatures [42] and [43]. In order to overcome the slight inclination and unevenness of GIF facet, a cylindrical base of height  $h_0 = 20 \mu\text{m}$  was added below the KSZP. Figure 1(b) shows the phase distributions and 3D profiles of different KSZP ( $\ell = -1, 0, 1, 2$ ) microstructure. The diameter and maximum height of KSZP microstructures are  $62.5 \mu\text{m}$  and  $23.23 \mu\text{m}$ , respectively. The output characteristics of these all-fiber generators can be adjusted by varying the structural parameters of KSZP.

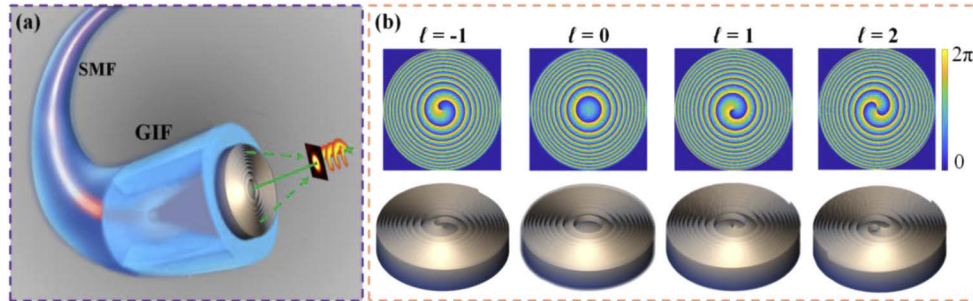


**Fig. 1.** (a) Schematic illustration of all-fiber focused vortex beam generator. (b) (up row) Phase profiles of the KSZP with different microstructure topological charge ( $\ell = -1, 0, 1,$  and  $2$ ) and (down row) the corresponding computer-aided design 3D profiles of the KSZP with a cylindrical base.

We fabricated KSZP microstructure on the GIF facet by using a commercially available nanoprinting system (Photonic Professional GT, Nanoscribe GmbH) [40]. As shown in Fig. 2(a), the printing laser (780 nm center wavelength,  $\sim 100 \text{ fs}$  pulse width, and 80 MHz pulse repetition rate) was focused into the IP-L780 photoresist with an oil immersion objective (Carl Zeiss,  $63\times$ , NA = 1.4). The composite fiber structure was fixed with a homemade fiber holder and one can adjust the distance between the GIF facet and the thin microscope coverslip with micrometer precision. The IP-L780 photoresist and the index-matching oil were deposited on both the upper

and lower surfaces of the microscope coverslip with 170  $\mu\text{m}$  thick, respectively. The KSZP polymerization is completed using the layer-by-layer writing method based on galvo-mirror scanning mode. The optimal processing parameter was 50 mW laser power, 10000  $\mu\text{m}/\text{s}$  scan speed, 100 nm slicing space and hatching space. The writing time of single KSZP sample was about 14 minutes. The polymerized sample was first developed by immersing it in a propylene glycol methyl ether acetate (PGMEA) bath for 30 minutes to remove any unexposed residue, and the sample was subsequently placed in a second beaker with isopropanol for approximately 5 minutes. Finally, the fabricated microstructure was gently blown dry with nitrogen. The polymerized KSZP ( $\ell = -1, 0, 1$  and 2) samples are in good agreement with the design geometry according to the scanning electron microscopy (SEM) images [Figs. 2(b)–2(e)].

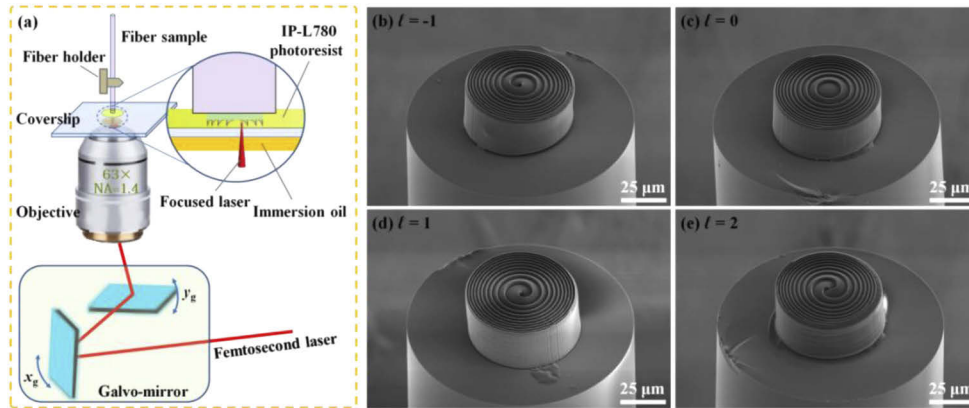


**Fig. 2.** (a) Schematic illustration of the 3D nanoprinting system. (b-e) SEM images of the nanoprinted KSZP microstructure with topological charge  $\ell = -1, 0, 1$  and 2, respectively.

### 3. Characterization

#### 3.1. Focal spot, focal length and vortex topological charge

The output light field characteristics of the KSZP samples were investigated based on the experimental setup shown in Fig. 3. A laser source with 1550 nm emission wavelength was connected to an optical fiber coupler with a splitting ratio 50/50, and then the beam was split into two branches (A and B). The two beams were coupled into a SMF through a bare fiber adapter and magnified with a 20 $\times$  objective lens, respectively. The magnified beam of the B branch passed through a polarizer ( $P_1$ ) and quarter-wave plate ( $QWP_1$ ). Subsequently, it was coupled into the front end (or the virgin end) of KSZP sample via a 20 $\times$  objective lens. The polarization state of the beam incident into the KSZP sample was adjusted by changing the angle between the polarizing direction of the  $P_1$  and the fast axis direction of the  $QWP_1$ . The rear end of KSZP sample was fixed on a translation stage, which allows one to horizontally move the sample end with micron-level precision. Since the intensity profile of the output beam of the KSZP sample can be projected into the infrared CCD camera via a 20 $\times$  objective, this setup can capture the intensity profile images at different horizontal positions when the A beam was blocked and the translation stage was adjusted. As a reference beam, the A beam passed through a mirror, tunable diaphragm and beam splitter, and then formed a coaxial interference pattern with the output beam of the KSZP sample. The interference pattern can also be imaged using the infrared CCD camera, which was used to test the vortex topological charge of the output beam from the KSZP sample.

In order to investigate the focal spot profile of different KSZP samples, we performed numerical simulations relying on the finite-difference time-domain (FDTD) algorithm. In simulation, the

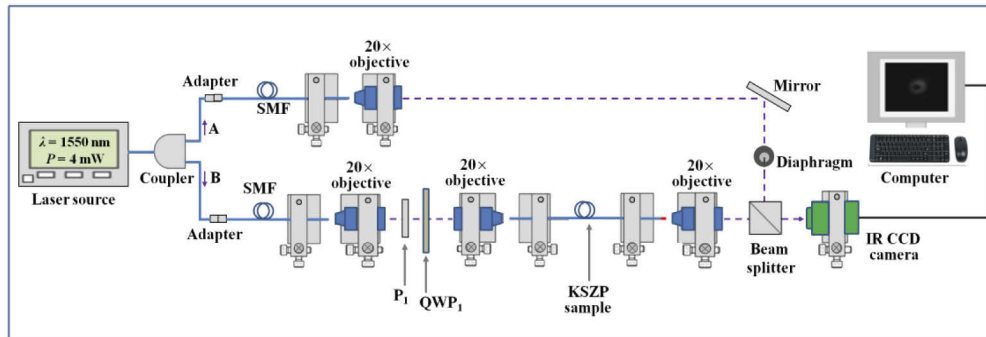


**Fig. 3.** Schematic illustration of the dual-beam interference microscopic imaging system.

linearly polarized (LP), left-handed circularly polarized (LCP) and right-handed circularly polarized (RCP) Gaussian beam with a wavelength of 1550 nm and a beam waist of 10  $\mu\text{m}$  were set as the incident light, impinging onto the KSZP microstructure at normal incidence, respectively. Similarly, other simulation parameters such as the focal length, refractive index and effective size of KSZP microstructure were set to be consistent with the experiment. Figures 4(a)–4(d) show the focal spot profiles of different sample ( $\ell = -1, 0, 1, 2$ ) from the numerical simulations and experimental measurements under different polarized light incident conditions (LP, LCP, and RCP). Meanwhile, the measured coaxial interference patterns are also presented in the bottom row of each sub-image in Fig. 4.

The focal spot profile obtained from the numerical simulation matches well with the measurement results. Here, the slight deviation is mainly caused by the processing quality of KSZP samples. In addition, we can also see that the polarization characteristics of incident light hardly affect the focal spot profile. For the case of  $\ell = 0$ , the output beam is focused into a Gauss-like spot, and this situation corresponds to the focusing effect of a traditional kinoform lens. For the case of  $\ell = -1, 1$ , and 2, the output beams are focused into a doughnut-like profile, respectively. Moreover, as  $|\ell|$  increases, the diameter of focal spot becomes larger. Quantitatively, the diameter of the Gauss-like spot in simulation is  $\sim 3.0 \mu\text{m}$ . However, the doughnut-like diameters are  $\sim 5.2 \mu\text{m}$  and  $\sim 6.8 \mu\text{m}$  for  $\ell = \pm 1$  and  $\ell = 2$ , respectively. Corresponding to  $\ell = -1, 0, 1$ , and 2, the diameters of the focal spots measured from the experiment were about 5.4, 3.1, 5.4 and 6.9  $\mu\text{m}$  respectively, which nicely matched with their simulation counterparts. The slight deviation mainly comes from the processing errors of KSZP samples and the measurement errors. In addition, the focal lengths in simulation are about 26.3, 26.8, 26.3, and 25.1  $\mu\text{m}$  for the case of  $\ell = -1, 0, 1$ , and 2, respectively. The corresponding measurement results are about 26.2, 27.4, 26.5, and 24.8  $\mu\text{m}$ , respectively. Here the big difference between the simulated (or measured) focal length and the designed focal length ( $f = 30 \mu\text{m}$ ) might be attributed to the processing quality and the diffraction of the evanescent fields inside the subwavelength features of KSZP microstructure [44].

The coaxial interferograms (Interf.) are shown in the bottom row of each sub-image in Fig. 4. Theoretically, in the interferograms the presence of the spiral arm shows that the output beam carries spiral phase and OAM. The number of spiral arms is equal to the vortex topological charge carried by the output beam. As shown in Fig. 4, when  $\ell = 0$ , the coaxial interferogram exhibits a Newton-ring-like fringe pattern, so there is no spiral arms and the output beam does not carry spiral phase and OAM. Its vortex topological charge value is equal to zero. When  $\ell = -1$  and 1, the coaxial interferogram exhibits single spiral arm pattern and their spiral arms rotate in the opposite direction. It can be concluded that the output beams of these two cases carry helical phase and OAM, but the vortex topological charges are opposite to each other. The number of spiral arms will increase as the value of  $|\ell|$  increases, which is supported by

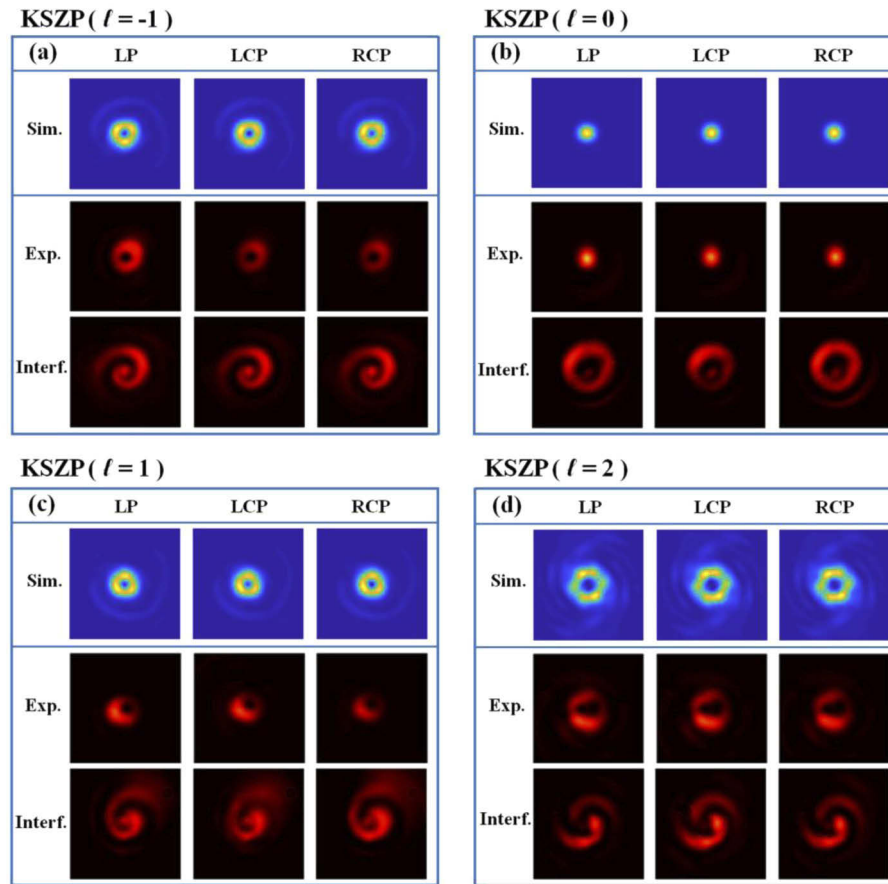


**Fig. 4.** Focal spot profiles obtained from FDTD simulation (top row) and experimental measurement (middle row), and the experimentally measured coaxial interference patterns (bottom row).

the measurement results for the case of  $\ell = 2$ . Essentially, these optical characteristics of this kind of all-fiber vortex beam generator can be easily controlled by flexibly adjusting the design parameters of KSZP microstructure. In addition, it is also worth mentioning that all vortex focusing characteristics, including the focal spot, focal length and vortex topological charge, are insensitive to the polarization state of incident beam.

### 3.2. Focusing efficiency and vortex purity

The focusing efficiency of the KSZP sample can be defined as the total intensity at the focus divided by the total intensity incident on the optic, times 100%. Here, we first measured the transmission loss of all samples using an optical power meter with nanowatt-level accuracy (PM122D, thorlabs). Results show that transmission losses of all samples are negligible. So the total intensity of the output beam of different KSZP sample is equal to its total intensity of entire incident beam. In addition, the KSZP only produce a single focus spot and its output beam does not include zero-order and extra multiple high-order diffraction. According to these two reasons, one can directly calculate the focusing efficiency of KSZP sample based on the photon response counting of the captured images on the focal plane. Taking the KSZP ( $\ell = -1$ ) sample under LP light incidence as an example, as shown in Fig. 5(a), we define the ratio of the photon response

count  $N_1$  of the circular area A covering the doughnut-like spot to the photon response count  $N_2$  of the circular area B with a diameter of 5 times A, times 100% as the focusing efficiency. Here,  $N_1$  corresponds to the total intensity at the focus, and  $N_2$  corresponds to the total intensity incident on the optic. And then, the focusing efficiency of KSZP sample was calculated using the expression:  $\eta = N_1 / N_2 \times 100\%$ . Figure 5(b) shows the calculated focusing efficiency of different samples ( $\ell = -1, 0, 1, 2$ ) under different polarized light incident conditions (LP, LCP, and RCP).

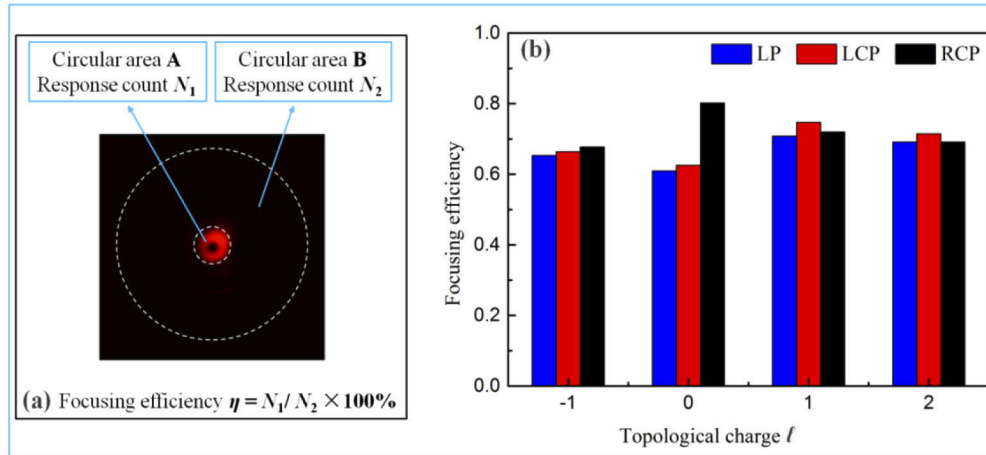


**Fig. 5.** (a) Schematic illustration of the calculation rule of focusing efficiency. (b) Focusing efficiency of different KSZP samples ( $\ell = -1, 0, 1$ , and 2) under different polarized light incident conditions (LP, LCP, and RCP).

Under different polarized light incidence (LP, LCP, and RCP), the focusing efficiency of the sample ( $\ell = -1$ ) are 0.6530, 0.6639, and 0.6777, respectively; the focusing efficiency of the sample ( $\ell = 0$ ) are 0.6093, 0.6258, and 0.8021, respectively; the focusing efficiency of the sample ( $\ell = 1$ ) are 0.7083, 0.7473, and 0.7197, respectively; the focusing efficiency of the sample ( $\ell = 2$ ) are 0.6916, 0.7148, and 0.6913, respectively. The focusing efficiency of all samples are above 60%. Here, the failure to achieve 100% focusing efficiency of the ideal KSZP is mainly attributed to the fact that the slicing and hatching space (100 nm) are not infinitely small in the nanoimprint processing. In addition, the nanoimprint accuracy and measurement errors also have an important impact on the final result. Except for  $\ell = 0$ , the focusing efficiency of other samples ( $\ell = -1, 1, 2$ ) is almost independent of the polarization state of incident light. There is a significant deviation in the focusing efficiency of the sample ( $\ell = 0$ ) when RCP is incident. The reason may be attributed to an accidental interference from external vibration during the experimental measurement. In view of the above measurement results, it can be concluded that the focusing efficiency of all samples are polarization insensitive.

Under different polarized light incidence, the vortex purity of the output beam of all samples was measured using the mode decomposition method. As shown in Fig. 6, the laser source have a wavelength of 1550 nm and power of 4 mW. The output beam from the KSZP sample was incident on a reflective phase-only liquid crystal spatial light modulator (SLM) after sequentially passing through a 20 $\times$  objective, quarter-wave plate (QWP<sub>2</sub>) and polarizer (P<sub>2</sub>). A Damman vortex grating hologram generated from our homemade MATLAB code was loaded into the SLM, and its specific phase profile can be seen from the dotted box content in Fig. 6. In order to investigate the vortex purity under different polarized light incidence, the polarization directions of the P<sub>1</sub> and P<sub>2</sub> were fixed and consistent with the polarization response direction (vertical direction) of SLM. Adjusting QWP<sub>1</sub>, the incident light irradiated into the KSZP sample can be set to a linearly polarized (LP), left-handed circularly polarized (LCP) and right-handed circularly

polarized (RCP) states, respectively. Under different polarized light incident situations, the fast axis direction of  $QWP_2$  was adjusted to an angle of  $+45$  and  $-45$  degrees (-L, -R) with the vertical direction in turn.

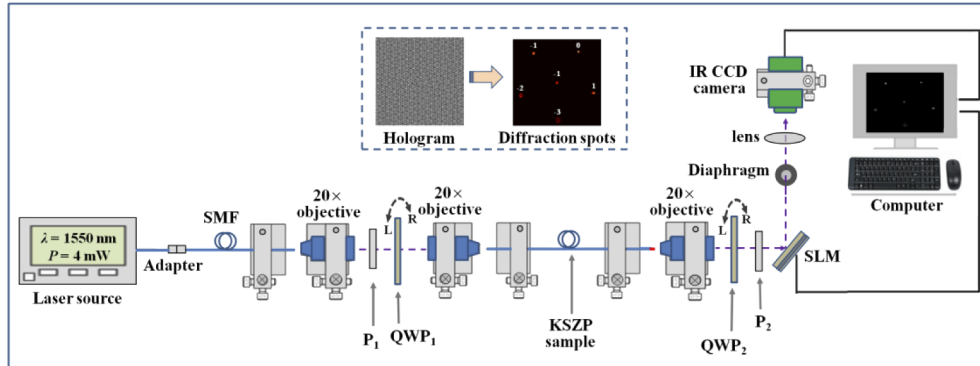


**Fig. 6.** Experimental setup for measuring the vortex purity of output beams.

When a Gaussian beam is incident onto the SLM, the loaded phase hologram will modulate the incident Gaussian beam into six different beams. Among them, five beams are vortex beams carrying the same energy and different vortex topological charge value  $p$ . The five beams are focused to five vertex positions of an equilateral pentagon via the same Fourier transform lens, respectively. Along the counterclockwise direction, the vortex topological charge values carried by the five focus spots are 2, 1, 0, -1, and -2, respectively. The remaining beam is not modulated by the hologram, so its characteristics are the same as those of the incident beam. The unmodulated beam is focused into the center position of the equilateral pentagon via the Fourier transform lens. Intensity distribution images of the six focus spots can be captured by the infrared CCD camera. Figure 7(a) shows the intensity distribution of the six focus spots. When  $p \neq 0$ , the focus spot presents a doughnut-like ring profile. However, the focus spot presents a Gaussian-like profile when  $p = 0$ .

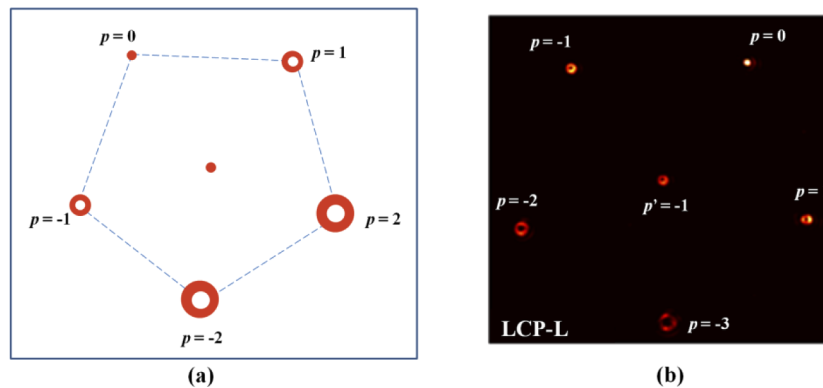


**Fig. 7.** Schematic diagram of the focus spot distribution (a) generated by the Gaussian beam and (b) generated by the output beam of the KSZP ( $l=1$ ) sample.

In order to clearly present the modulation effect of the SLM hologram, here we only take the KSZP ( $l = -1$ ) sample under the LCP-L incident condition as an example for detailed explanation. The output beam of the KSZP ( $l = -1$ ) sample mainly carries vortex topological charge value  $p' = -1$ . As a result, when the vortex beam generated from the KSZP sample carries vortex

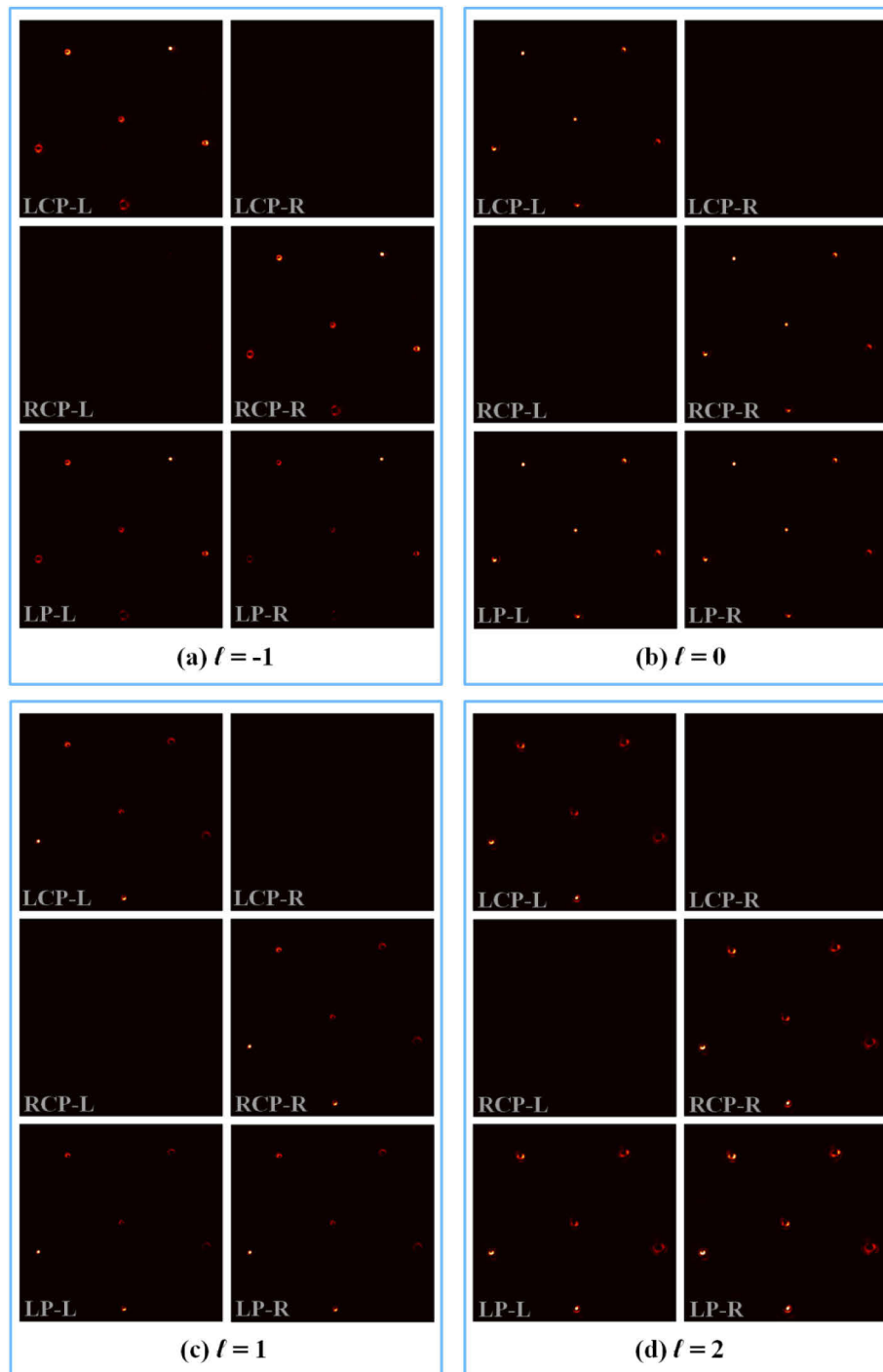


**Fig. 8.** Light intensity distribution images modulated by SLM hologram under different incident conditions (LCP-L, LCP-R, RCP-L, RCP-R, LP-L, and LP-R)

topological charge  $p'$  component that is conjugate with the vortex topological charge at one of the vertices of the above equilateral pentagon [see Fig. 7(a)], the doughnut-like ring spot profile at the special vertex can be modulated into a Gauss-like spot. Meanwhile, the beams at other vertices can be modulated into doughnut-like ring spots. The new topological charges carried by the focus spots at different vertex positions are the sum of their original value and the topological charge value carried by the output beam of KSZP sample. It is worth noting that the vortex topological charge  $p$  of the focus spot at the center of the equilateral pentagon is always consistent with that of the incident vortex beam from the KSZP sample. Figure 7(b) shows all the focus spot images of the KSZP ( $\ell = -1$ ) output beam after being modulated by the SLM hologram. Along the counterclockwise direction, new vortex topological charge values carried by these focal spots at the five vertex positions are 1, 0, -1, -2, and -3, respectively. The vortex topological charge of the focus spot at the center of the pentagon is consistent with that of the incident vortex beam from the KSZP sample, and  $p' = -1$ . For different samples, all light intensity distribution images modulated by SLM hologram under different incident conditions (LCP-L, LCP-R, RCP-L, RCP-R, LP-L, and LP-R) are shown in Fig. 8, respectively, and these modulated images are consistent with our design.

Under the two incident conditions (LCP-R, RCP-L), the light field intensity is almost zero, and this result proves the polarization independent characteristics of the KSZP samples once again. For any KSZP sample, the vortex topological charge carried by the output beam can not be unique due to the influence of structural machining errors and other factors. That is, the output beam often carries other vortex topological charge components. The contribution of each vortex topological charge component to the entire output vortex beam was measured by recording the photon response counts in the center region of the five vertex positions of converted optical field. The purity of the output vortex beam in a specific topological charge component was then determined by calculating the ratio of the photon response count in the center region of the corresponding focus spot position to the sum of the photon response counts in the center region of all focus spot positions.

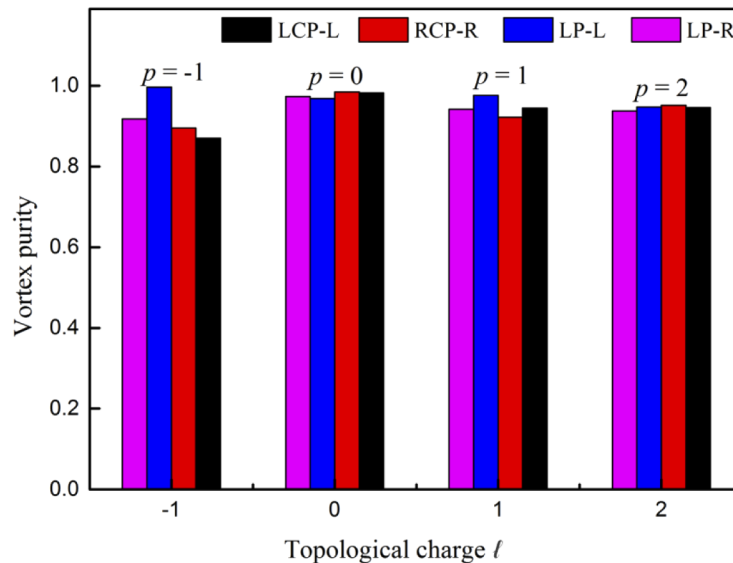


**Fig. 9.** Vortex purity of output beams for different samples under different polarized light incident conditions.

The purity of the output beam of all KSZP ( $\ell = -1, 0, 1, 2$ ) samples at the designed vortex topological charge  $p = \ell$  component was calculated using the method described in the previous paragraph, and all calculation results are shown in the histogram in Fig. 9. For different incident conditions (LCP-L, RCP-R, LP-L, and LP-R), the purity of the vortex topological charge ( $p = -1$ ) component are 0.8697, 0.8951, 0.9961, and 0.9179 for the KSZP sample with  $\ell = -1$ , respectively. The vortex purity of  $p = 0$  component are 0.9823, 0.9846, 0.9685, and 0.9731 for the KSZP sample with  $\ell = 0$ , respectively. The purity of  $p = 1$  component are 0.9442, 0.9222, 0.9763, and 0.9415 for the KSZP sample with  $\ell = 1$ , respectively. The purity of  $p = 2$  component are 0.9460, 0.9512, 0.9476, and 0.9371 for the KSZP sample with  $\ell = 2$ , respectively. Above data shows that, under different polarization states of the incident beam, all samples maintain high vortex purity ( $> 86\%$ ) at the designed vortex topological charge ( $p = \ell$ ) component. Moreover, the polarization state of incident beam has very little effect on the vortex purity value. Here the reason why the vortex purity cannot reach 100% can be attributed to the combined effect of many factors such as the measurement error, machining error and limited nanoimprint accuracy.

#### 4. Conclusions

In summary, we have proposed and demonstrated that integrating a KSZP on the top of the composite fiber structure composed of a single mode fiber and a quarter pitch graded index fiber could realize a high-efficiency all-fiber focused vortex beam generator. Under different polarization incidence, its output light field characteristics from experimental measurements are in good agreement with that of theoretical prediction. In addition, this fiber optic devices can be considered as a polarization-independent focused vortex beam generator. The focusing efficiency and vortex purity are better than 60.09% and 86.97%, respectively, which benefits from the excellent focus conversion efficiency of KSZP. Moreover, the conversion efficiency of this generator will get closer to 100% if we further optimize the processing parameters including laser energy, scanning speed, slicing and hatching space. Due to the high conversion efficiency, the all-fiber generators have the promising potential for enabling new types of low power consumption fiber devices in optical communication and optical manipulation applications.

#### Funding

National Natural Science Foundation of China (61425007, 61875134, 61905155, 61905166, 61935013); Science and Technology Innovation Commission of Shenzhen (KQJSCX20170727101953680)

#### Acknowledgments

All authors are very grateful to the Photonics Research Centre of Shenzhen University for supplying the experimental Nanoscribe GmbH system. We are also grateful to the equipment administrator, Min Wang and Zhongyang Liu for their technical guidance in the use of equipment.

#### Disclosures

The authors declare no conflicts of interest.

#### References

1. A. M. Yao and M. J. Padgett, "Orbital angular momentum: Origins, behavior and applications," *Adv. Opt. Photonics* **3**(2), 161–204 (2011).
2. A. E. Willner, H. Huang, Y. Yan, Y. Ren, N. Ahmed, G. Xie, C. Bao, L. Li, Y. Cao, Z. Zhao, J. Wang, M. P. J. Lavery, M. Tur, S. Ramachandran, A. F. Molisch, N. Ashrafi, and S. Ashrafi, "Optical communication using orbital angular momentum beams," *Adv. Opt. Photonics* **7**(1), 66–106 (2015).
3. A. Trichili, C. Rosales-Guzmán, A. Dudley, B. Ndagano, A. B. Salem, M. Zghal, and A. Forbes, "Optical communication beyond orbital angular momentum," *Sci. Rep.* **6**(1), 27674 (2016).

4. M. A. Lauterbach, M. Guillon, A. Soltani, and V. Emiliani, "STED microscope with spiral phase contrast," *Sci. Rep.* **3**(1), 2050 (2013).
5. G. Vicidomini, P. Bianchini, and A. Diaspro, "STED super-resolved microscopy," *Nat. Methods* **15**(3), 173–182 (2018).
6. M. Padgett and R. Bowman, "Tweezers with a twist," *Nat. Photonics* **5**(6), 343–348 (2011).
7. J. P. Torres and L. Torner, *Twisted Photons: Applications of light with orbital angular momentum* (Wiley-VCH, Bristol: 2011).
8. M. J. Padgett and L. Allen, "Orbital angular momentum exchange in cylindrical-lens mode converters," *J. Opt. B: Quantum Semiclassical Opt.* **4**(2), S17–S19 (2002).
9. M. W. Beijersbergen, R. P. C. Coerwinkel, M. Kristensen, and J. P. Woerdman, "Helical-wavefront laser beams produced with a spiral phase plate," *Opt. Commun.* **112**(5-6), 321–327 (1994).
10. Y. C. Zhang, W. W. Liu, J. Gao, and X. D. Yang, "Generating focusing 3D perfect vortex beams by plasmonic metasurfaces," *Adv. Opt. Mater.* **6**(4), 1701228 (2018).
11. G. C. G. Berkhout, M. P. J. Lavery, J. Courtial, M. W. Beijersbergen, and M. J. Padgett, "Efficient sorting of orbital angular momentum states of light," *Phys. Rev. Lett.* **105**(15), 153601 (2010).
12. F. Ding, Y. T. Chen, and S. I. Bozhevolnyi, "Focused vortex-beam generation using gap-surface plasmon metasurfaces," *Nanophotonics* **9**(2), 371–378 (2020).
13. K. Ou, G. H. Li, T. X. Li, H. Yang, F. L. Yu, J. Chen, Z. Y. Zhao, G. T. Cao, X. S. Chen, and W. Lu, "High efficiency focusing vortex generation and detection with polarization-insensitive dielectric metasurfaces," *Nanoscale* **10**(40), 19154–19161 (2018).
14. S. Boichenko, "Toward super-resolution fluorescent microscopy of arbitrarily oriented single molecules," *Phys. Rev. A* **101**(4), 043823 (2020).
15. N. R. Heckenberg, R. McDuff, C. P. Smith, and A. G. White, "Generation of optical phase singularities by computer-generated holograms," *Opt. Lett.* **17**(3), 221–223 (1992).
16. A. Sakdinawat and Y. W. Liu, "Soft-x-ray microscopy using spiral zone plates," *Opt. Lett.* **32**(18), 2635–2637 (2007).
17. L. Kipp, M. Skibowski, R. L. Johnson, R. Berndt, R. Adelung, S. Harm, and R. Seemann, "Sharper images by focusing soft X-rays with photon sieves," *Nature* **414**(6860), 184–188 (2001).
18. Y. H. Liang, E. L. Wang, Y. L. Hua, C. Q. Xie, and T. C. Ye, "Single-focus spiral zone plates," *Opt. Lett.* **42**(13), 2663–2666 (2017).
19. R. V. Johnson and A. R. Tanguay Jr, "Stratified volume holographic optical elements," *Opt. Lett.* **13**(3), 189–191 (1988).
20. M. S. D. Smith and K. A. Mcgreer, "Diffraction gratings utilizing total internal reflection facets in Littrow configuration," *IEEE Photonics Technol. Lett.* **11**(1), 84–86 (1999).
21. Z. Y. Zhang, C. L. Guo, R. Q. Wang, H. X. Hu, X. G. Zhou, T. Liu, D. L. Xue, X. Zhang, F. Zhang, and X. J. Zhang, "Hybrid-level Fresnel zone plate for diffraction efficiency enhancement," *Opt. Lett.* **25**(26), 33676–33687 (2017).
22. H. Lajunen, J. Tervo, and J. Turunen, "High-efficiency broadband diffractive elements based on polarization gratings," *Opt. Lett.* **29**(8), 803–805 (2004).
23. S. Shrestha, A. C. Overvig, M. Lu, A. Stein, and N. F. Yu, "Broadband achromatic dielectric metalenses," *Light: Sci. Appl.* **7**(1), 85 (2018).
24. J. A. Jordan, P. M. Hirsch, L. B. Lesem, and D. L. Van Rooy, "Kinoform lenses," *Appl. Opt.* **9**(8), 1883–1887 (1970).
25. S. Gorelick, M. D. De Jonge, C. M. Kewish, and A. A. De Marco, "Ultimate limitations in the performance of kinoform lenses for hard x-ray focusing," *Opt. Express* **6**(6), 790–793 (2019).
26. M. Larsson, M. Ekberg, F. K. Nikolajeff, S. Hard, P. D. Maker, and R. E. Muller, "Proximity-compensated kinoforms directly written by e-beam lithography," *Proc. SPIE* **10271**, 1027109 (1993).
27. K. Keskinbora, C. Grévent, M. Hirscher, M. Weigand, and G. Schütz, "Single-step 3D nanofabrication of kinoform optics via gray-scale focused ion beam lithography for efficient X-ray focusing," *Adv. Opt. Mater.* **3**(6), 792–800 (2015).
28. K. Keskinbora, U. T. Sanli, C. Grévent, and G. Schütz, "Fabrication and x-ray testing of true kinoform lenses with high efficiencies," *Proc. SPIE* **9592**, 95920H (2015).
29. P. Vayalankuzhi, S. Bhattacharya, U. Eigenthaler, K. Keskinbora, C. T. Samlan, M. Hirscher, J. P. Spatz, and N. K. Viswanathan, "Direct patterning of vortex generators on fiber tip using a focused ion beam," *Opt. Lett.* **41**(10), 2133–2136 (2016).
30. Y. M. Lu, Z. N. Tian, S. N. Yang, J. C. Hua, X. Q. Liu, Y. Zhao, Q. D. Chen, Y. L. Zhang, and H. B. Sun, "High-efficiency spiral zone plates in Sapphire," *IEEE Photonics Technol. Lett.* **31**(12), 979–982 (2019).
31. X. Q. Liu, Q. D. Chen, K. M. Guan, Z. C. Ma, Y. H. Yu, Q. K. Li, Z. N. Tian, and H. B. Sun, "Dry-etching-assisted femtosecond laser machining," *Laser Photonics Rev.* **11**(3), 1600115 (2017).
32. J. K. Hohmann, M. Renner, E. H. Waller, and G. von Freymann, "Three-dimensional  $\mu$ -printing: an enabling technology," *Adv. Opt. Mater.* **3**(11), 1488–1507 (2015).
33. V. Hahn, S. Kalt, G. M. Sridharan, M. Wegener, and S. Bhattacharya, "Polarizing beam splitter integrated onto an optical fiber facet," *Opt. Express* **26**(25), 33148–33157 (2018).
34. T. Gissibl, S. Thiele, A. Herkommer, and H. Giessen, "Two-photon direct laser writing of ultracompact multilens objectives," *Nat. Photonics* **10**(8), 554–560 (2016).

35. T. Gissibl, M. Schmid, and H. Giessen, "Spatial beam intensity shaping using phase masks on single-mode optical fibers fabricated by femtosecond direct laser writing," *Optica* **3**(4), 448–451 (2016).
36. S. Juodkazis, V. Mizeikis, K. K. Seet, M. Miwa, and H. Misawa, "Two-photon lithography of nanorods in SU-8 photoresist," *Nanotechnology* **16**(6), 846–849 (2005).
37. K. Sugioka and Y. Cheng, "Ultrafast lasers-reliable tools for advanced materials processing," *Light: Sci. Appl.* **3**(4), e149 (2014).
38. Z. N. Tian, Q. D. Chen, Z. Y. Hu, Y. K. Sun, Y. H. Yu, H. Xia, and H. B. Sun, "Mirror-rotation-symmetrical single-focus spiral zone plates," *Opt. Lett.* **43**(13), 3116–3119 (2018).
39. Z. Y. Hu, Z. N. Tian, J. G. Hua, Q. D. Chen, and H. B. Sun, "Axially controllable multiple orbital angular momentum beam generator," *Appl. Phys. Lett.* **117**(2), 021101 (2020).
40. Z. W. Xie, S. C. Gao, T. Lei, S. F. Feng, Y. Zhang, F. Li, J. B. Zhang, Z. H. Li, and X. C. Yuan, "Integrated (de)multiplexer for orbital angular momentum fiber communication," *Photonics Res.* **6**(7), 743–749 (2018).
41. X. Z. Xu, J. He, M. X. Hou, S. Liu, Z. Y. Bai, Y. Wang, C. R. Liao, Z. B. Ouyang, and Y. P. Wang, "A Miniature Fiber Collimator for Highly Sensitive Bend Measurements," *J. Lightwave Technol.* **36**(14), 2827–2833 (2018).
42. T. Gissibl, S. Wagner, J. Sykora, M. Schmid, and H. Giessen, "Refractive index measurements of photoresists for three-dimensional direct laser writing," *Opt. Mater. Express* **7**(7), 2293–2298 (2017).
43. Y. Li, S. Park, M. McLamb, M. Lata, S. Schöche, D. Childers, I. D. Aggarwal, M. K. Poutous, G. Boreman, and T. Hofmann, "UV to NIR optical properties of IP-Dip, IP-L, and IP-S after two-photon polymerization determined by spectroscopic ellipsometry," *Opt. Mater. Express* **9**(11), 4318–4328 (2019).
44. H. J. Lezec and T. Thio, "Diffracted evanescent wave model for enhanced and suppressed optical transmission through subwavelength hole arrays," *Opt. Express* **12**(16), 3629–3651 (2004).